J Mater Sci (2020) 55:748–761

Metals & corrosion

Study on dynamic mechanical properties and constitutive model of ^{10}B/Al composite compared with its matrix of high-purity aluminum

Xingjun Wang[1], Feng Jiang[2,*], Tao Zhang[2], and Liping Wang[3,*]

[1] *School of Mechanical and Electrical Engineering, University of Electronic Science and Technology of China, Chengdu 611731, People's Republic of China*
[2] *Institute of Manufacturing Engineering, Huaqiao University, Xiamen 361021, People's Republic of China*
[3] *Department of Mechanical Engineering, Tsinghua University, Beijing 100084, People's Republic of China*

Received: 7 May 2019
Accepted: 20 August 2019
Published online: 27 August 2019

© Springer Science+Business Media, LLC, part of Springer Nature 2019

ABSTRACT

The dynamic mechanical properties of ^{10}B/Al composite have been tested by split Hopkinson pressure bar. High-purity aluminum, the matrix of composite, has been tested as the comparison with ^{10}B/Al composite. The scope of strain rate is from about 3000 s^{-1}–12000^{-1}, and the temperature scope is from room temperature to 350 °C. The true strain–stress curves have been obtained. The sensitivity of strain rates and temperatures on the true stress of ^{10}B/Al composite and high-purity aluminum has been analyzed. The true stress of the ^{10}B/Al composite material is 50% higher than that of pure aluminum. The strain rate sensitivity of ^{10}B/Al composite material is less than that of pure aluminum. The true stress of ^{10}B/Al composite material drops obviously when temperature is higher than 250 °C, due to the interface fracture between particles and matrix, and the movement of boron particles. The adiabatic temperature rise due to material deformation has been calculated, considering the heat capacity with the various temperatures. The total temperature due to plastic deformation of the ^{10}B/Al composite material is 41% higher than that of pure aluminum. The constitutive equations based on power-law and Johnson–Cook models have been introduced to characterize the dynamic mechanical properties of materials under different temperature and strain rates. The fitting results of the two constitutive models are compared with the experimental results. The fitting accuracy of the Johnson–Cook model is higher than that of pow-law model.

Address correspondence to E-mail: jiangfeng@hqu.edu.cn; Lpwang@tsinghua.edu.cn

https://doi.org/10.1007/s10853-019-03949-z

List of symbols

D	Specimen diameter
L_0	Specimen length
E	Elastic modulus of bar
A_0	Cross-sectional area of bar
A	Cross-sectional area of the specimen
ε_r	Amplitude of the reflected strain
ε_t	Amplitude of transmitted strain
C_0	One-dimensional elastic wave velocity
ρ_0	Density of bar
σ_T	True stress
ε_T	True strain
N	Strain hardening exponent
M	Strain rate hardening exponent
c_0–c_3	Material constants
σ_0	Yield strength
$\dot{\varepsilon}$	Strain rate
ΔT	Adiabatic temperature
ρ	Density of the material
C_p	Specific heat capacity
β	Energy conversion rate
T_{def}	Total deformation temperature
T_{room}	Room temperature
Θ	Thermal softening coefficient
σ_i	Isothermal stress
A	Yield strength
B	Strain hardening coefficient
C	Strain rate hardening coefficient
n	Strain hardening exponent
m	Thermal softening exponent
T_{melt}	Melt point

Introduction

The material research from monolithic to composite materials is a trend in the past 10 years. Among various composite materials, aluminum matrix composite is very popular due to the lightweight of aluminum as the matrix and the wide selection of reinforced particles. And reinforcements like particulate alumina, silicon carbide, graphite, fly ash, etc., can easily be incorporated in the melt using cheap processing methods. The additive of alumina, silicon carbide, etc., could increase the material strength [1], while the additive of graphite, boron carbide, etc., could improve the tribological properties [2]. Besides, some additives in the aluminum matrix composite could result in some special material performance [3]. The additive of boron into aluminum matrix realizes the material properties of high thermal neutron absorption cross section and wide absorption neutron energy range, which can be used to simulate the helium damage behavior of materials [4]. The B/Al composite parts with the requirement of high geometrical precision and surface quality are widely used in the physical experiments to enhance the experimental accuracy. The ultra-precision manufacturing of B/Al composite parts is a big challenge due to the local high hardness, nonuniform material flow and higher cutting temperature. In addition,boron particles doped in aluminum have an important influence on the wear of cutting tools during the ultra-precision cutting process [5]. So the understanding of material deformation mechanism is the basis of ultra-precision manufacturing of B/Al composite parts.

In recent years, researchers have realize that the inherent relationship between the material deformation mechanism and the dynamic mechanical properties of materials. Material constitutive models have been widely used to describe the plastic behavior of materials over the decades. Macroscopic constitutive descriptions could be divided into constitutive models based on physic and phenomenon [6]. Physic-based constitutive models account for physical aspects of the material behavior, and phenomenon-based constitutive models usually derive from empirical observations. Phenomenon-based constitutive models consist of fewer material constants compared with physic-based constitutive models, which makes it easier to be developed and more widely used in the process of cutting, forming, welding and impact [7]. Johnson–Cook model and power-law model are most widely used constitutive models [8]. The material removal and related physical phenomena during cutting processing are studied by characterizing the dynamic mechanical properties of the materials. Modeling and simulation of the machining processes has become a key method in the machinability assessment of difficult-to-cut workpiece materials [9]. Ghandehariun et al. presented a novel comprehensive constitutive equation, which is used on machining modeling of metal matrix composite. The particle size and volume fraction of metal matrix composite have been explicitly included as control parameters of constitutive equation [10]. Zhang et al. considered the influence of high temperature on the

constitutive model of Al/SiCp/45 metal matrix composite. It has been employed for the modeling of saw-tooth chip formation during laser-assisted machining process. Especially for metal matrix composites, the additive of hard particle influences the true stress, as well as the failure criteria of materials. So the interface between particles and matrix is a hot research topic [11]. Zhou et al. built the elastic–plastic constitutive model and Johnson–Cook damage model for the Al alloy matrix and the elastic-brittle failure for SiC particle to simulate the machining of high-volume fraction SiCp/Al composite and analyze the machinability of high-volume fraction SiCp/Al composite [12]. Xu et al. built the cutting modeling of hybrid CFRP/Ti composite with induced damage model. The numerical results highlighted the pivotal role of the affected interface zone in affecting the formation of interface delamination and the significant impacts of feed rate and cutting speed on delamination extent and fiber/matrix failure [13].

However, the mechanism of particle movement related to metal matrix is not clear. And the temperature during aluminum matrix composite deformation is seldom considered, which is very important for the geometrical precision of machined parts. In this study, the impact compression of ^{10}B/Al composite and its matrix of high-purity aluminum materials under different strain rates and different temperatures have been performed by split Hopkinson pressure bar (SHPB). The stress–strain curves under different strain rates and temperatures have been obtained. The adiabatic temperature rise due to material deformation has been calculated, considering the heat capacity with the various temperatures. The differences between ^{10}B/Al composite and its matrix of high-purity aluminum have been analyzed. The constitutive equations based on power-law and Johnson–Cook models have been introduced to characterize the dynamic mechanical properties of materials under different temperature and strain rates. The fitting results of the two constitutive models are compared with the experimental results.

Materials and experiments

Materials and samples

The material selected in this experiment is ^{10}B/Al composite, whose matrix is high-purity aluminum, which is selected as the comparison. The ^{10}B/Al composite is manufactured by adding ^{10}B powder (mass ratio 0.13%) into high-purity aluminum, and its metallographic SEM image is shown in Fig. 1a. It is found that the boron particle is strip shaped and the grain size of purity aluminum matrix is about 25 μm. The surface of ^{10}B/Al composite is processed by focused ion beam (FIB) technology to investigate the interface between particle and matrix, as shown in Fig. 1b. It is found that the contact between particle and matrix is compass. The grain of purity aluminum matrix near the interface between particle and matrix is obviously refined, even smaller than 1 μm. The refinement is gradual from the interface to the matrix. It is different from other aluminum matrix composite, like Si/Al [14] or SiC/Al composite [15].

The optimum length–diameter ratio of the sample could minimize the error caused by the inertial effect [16]. The length–diameter ratio of the experimental sample is designed to 1, where specimen diameter D is Φ2 mm and the length L_0 is 2 mm. In order to meet the stress homogeneity of the split Hopkinson bar and to reduce the influence of the friction between the rods and the specimens [17], the two end faces of the cylinder specimen were finished to ensure that the parallelism of two end faces is less than 0.01 mm, while their perpendicularity with the axis is less than 0.01 mm. And the average surface roughness is lower than 0.32 μm.

SHPB tester and principle

Split Hopkinson pressure bar (SHPB) technique is the commonly used method for material dynamic mechanical properties [18, 19] with the strain rate range of 10^2–10^4 s^{-1} [20]. As shown in Fig. 2, the specimen is sandwiched between two bars, where one is the incident bar and the other is the transmitted bar. The strike bar impacts the incident bar, and the stress wave is generated. The specimen is deformed plastically due to the cyclic load of stress wave. The strain gauges located on the incident bar and transmitted bar record the elastic strain of bars and then solve the stress–strain curves during the impact procedure.

The relationship between strain ε and strain rate $\dot{\varepsilon}$ with time is presented as follows:

$$\sigma(t) = EA\varepsilon_t(t)/A_0 \quad (1)$$

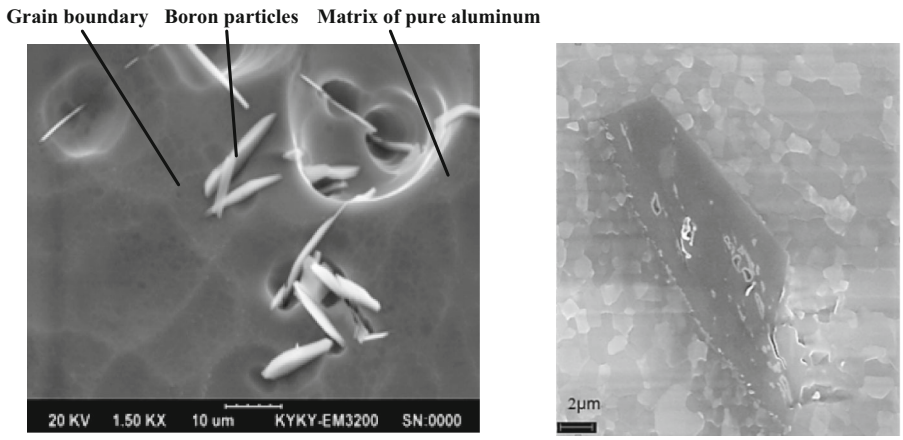

(a) The metallographic SEM image **(b)** The interface between particle and matrix

Figure 1 The microstructure of ^{10}B/Al composite.

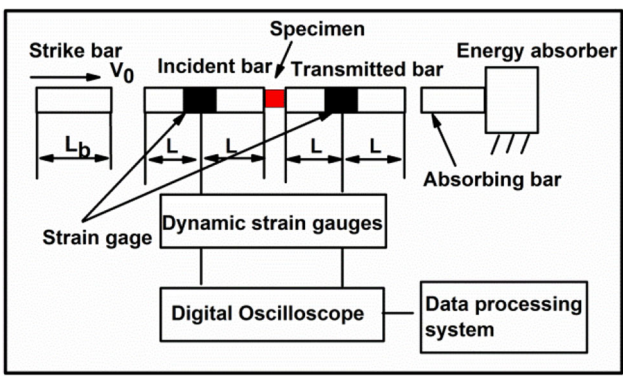

Figure 2 The diagram of split Hopkinson pressure bar.

$$\varepsilon(t) = -\frac{2C_0}{L_0}\int_0^t \varepsilon_r(t)\,\mathrm{d}t \tag{2}$$

$$\dot{\varepsilon} = -2C_0\varepsilon_r/L_0 \tag{3}$$

where σ is the engineering stress, E is the elastic modulus of the bars, A_0 is the cross-sectional area of the bars, whose diameter is 5 mm, A is the cross-sectional area of the sample, ε_t is the amplitude of transmitted strain, L_0 is the length of the sample. ε_r is the amplitude of the reflected strain wave, and C_0 is the one-dimensional elastic wave velocity of the bar, which could be presented as:

$$C_0 = (E/\rho_0)^{1/2} \tag{4}$$

where ρ_0 is the density of the bar.

The engineering stress and strain can be calculated from Eqs. (1)–(3). True stress σ_T and true strain ε_T are defined as the following relationships:

$$\sigma_T = (1-\varepsilon)\sigma \tag{5}$$

$$\varepsilon_T = -\ln(1-\varepsilon) \tag{6}$$

The original waveforms in each bar during the compression process of high-purity aluminum material are shown in Fig. 3.

Design of experiments

The influence of strain rates and temperatures on the SHPB tests is considered. The design of experiments is listed as given in Table 1.

However, the strain rates are calculated after tests. The strain rate depends on not only impact pressure, but also on the material hardening. So the calculated strain rates of ^{10}B/Al composite and high-purity aluminum with the same impact pressure could be of a slight difference.

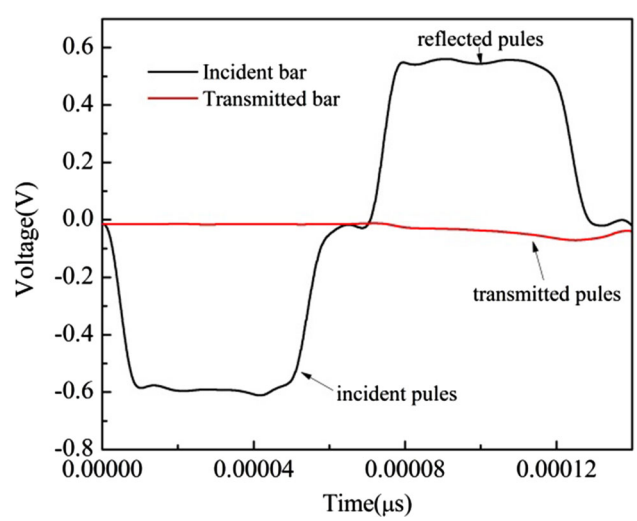

Figure 3 The original waveforms in the incident and transmitted bars, respectively.

Table 1 The design of SHPB experiments

Impact pressures (MPa)	Temperatures (°C)
0.04	Room temperature
	100
	150
	200
	250
	300
	350
0.08	Room temperature
0.12	
0.16	
0.20	Room temperature
	100
	150
	200
	250
	300
	350

The temperature given in Table 1 is the temperature of the cylindrical surface of specimen, which is measured by a thermal couple 1 mm near the cylindrical surface of specimen. So the heating time is set to 3 min to ensure the uniformity of specimens. And the adiabatic temperature rise could be considered due to short deformation time of specimen materials. The room temperature is 20 °C in this study.

The repeated time is two, but if these two results are not repeatable, additional test is repeated to ensure the repeatability of experimental results.

Results and discussion

Stress–strain curves in the different impact pressures and temperature

Figure 4a, b shows the true stress–strain curves of ^{10}B/Al composite and high-purity aluminum in the room temperature at different strain rates, respectively. It is found that the true stress increases nonlinearly with the increase in true strain. This phenomenon is called as work hardening, which indicates that the material enters the plastic deformation stage. The mechanism of work hardening of the material is due to the proliferation and interaction of dislocations during plastic deformation [21].

As shown in Fig. 4, it is found that the true stress of ^{10}B/Al composite is more than 50% higher than the pure aluminum. As mentioned in "Materials and samples" section, the additive of boron particle leads to the grain refinement of pure aluminum matrix near the particle–matrix interface, which improves the strength of composite.

Figure 5a, b shows the true stress–strain curves of ^{10}B/Al composite and high-purity aluminum at different temperatures in the strain rate of 3000 s^{-1}. Figure 6a, b shows the true stress–strain curves of ^{10}B/Al composite and high-purity aluminum at different temperatures in the strain rate of 12000 s^{-1}.

It is found that the thermal softening of ^{10}B/Al composite in the lower strain rate (3000 s^{-1}) is stronger than that of high-purity aluminum, especially in the temperature beyond 250 °C. The thermal softening of both ^{10}B/Al composite and high-purity aluminum is stronger when the strain rate is up to about 12000 s^{-1}. But the thermal softening of ^{10}B/Al composite is more obvious than that of high-purity aluminum in the high strain rate. The material plasticity decreases with the increase in temperature. The material plasticity almost does not change with the change of strain rates for ^{10}B/Al composite, while the material plasticity increases in the higher strain rate for high-purity aluminum, especially in the condition of high temperature.

The adiabatic temperature rise

The deformation process of material in the SHPB tests could be considered as the adiabatic condition. The adiabatic temperature rise during the dynamic deformation of material can be calculated by the following equation:

$$\Delta T = \frac{\beta}{\rho C_p} \int_0^{\varepsilon} \sigma \, d\varepsilon \tag{7}$$

where ρ is the density of the material, C_p is the specific heat capacity of the material, and β is the energy conversion rate. The density of high-purity aluminum and ^{10}B/Al composite is 2.6991 g/cm^3 and 2.6968 g/cm^3, respectively.

The specific heat capacity of materials is greatly affected by the temperature. So the specific heat capacity of ^{10}B/Al composite and high-purity aluminum has been tested at the temperature of room temperature, 100 °C, 150 °C, 200 °C, 250 °C, 300 °C and 350 °C, by the aid of laser thermal conductivity

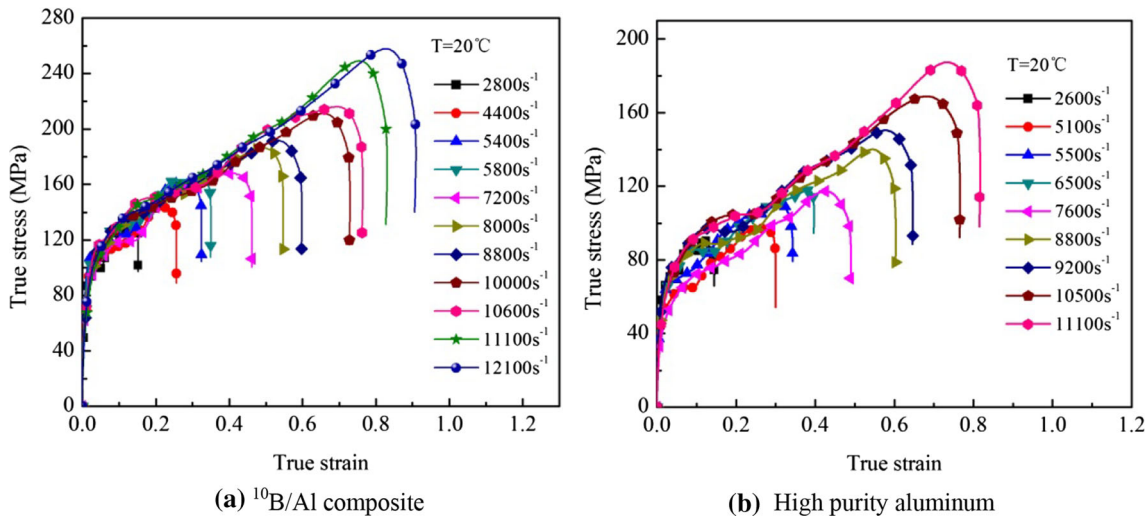

(a) ^{10}B/Al composite **(b)** High purity aluminum

Figure 4 The true strain–strain curves of different strain rates in the room temperature.

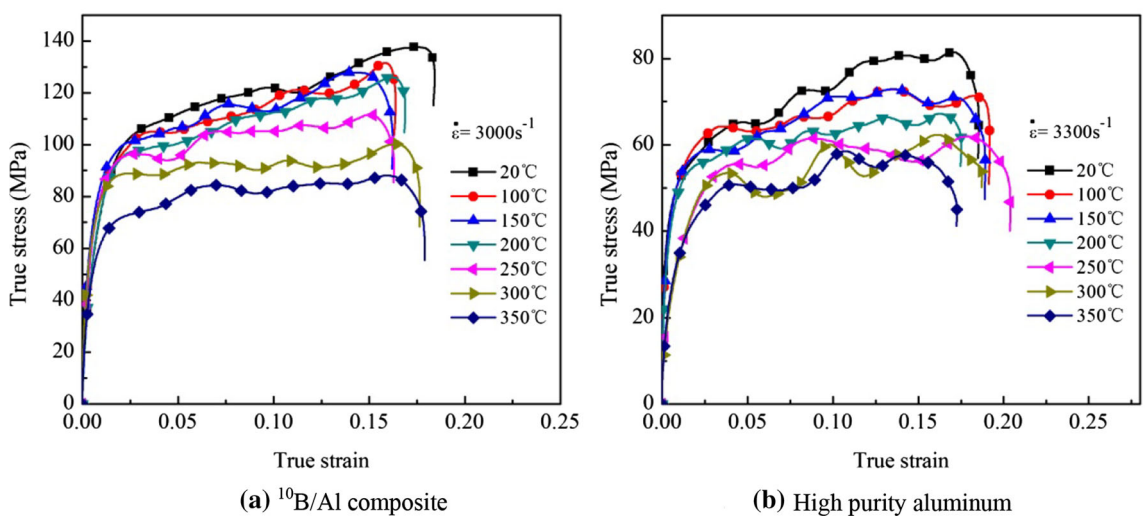

(a) ^{10}B/Al composite **(b)** High purity aluminum

Figure 5 The true strain–strain curves of different temperatures in the strain rate of 3000 s^{-1}.

meter (type NETZSCH LFA 457), as shown in Fig. 7a, b. The specific heat capacity of ^{10}B/Al composite and high-purity aluminum increases with the increase in temperature. And the specific heat capacity of ^{10}B/Al composite is a little lower than that of high-purity aluminum.

The temperature-depended specific heat capacity is fitted by polynomial equation to use in the calculation of adiabatic temperature rise. The mathematical expression for the relationship between specific heat capacity and temperature of ^{10}B/Al composite in the temperature range from room temperature to 350 °C is as follows:

$$C_p = 0.8279 + 0.0004T + 4e^{-7}T^2 - 6e^{-10}T^3 \quad 20\,^\circ\mathrm{C} \le T \le 350\,^\circ\mathrm{C} \tag{8}$$

The mathematical expression for the relationship between specific heat capacity and temperature of high-purity aluminum in the temperature range from room temperature to 350 °C is as follows:

$$C_p = 0.8736 + 0.0003T + 4e^{-7}T^2 + 3e^{-10}T^3 \quad 20\,^\circ\mathrm{C} \le T \le 350\,^\circ\mathrm{C} \tag{9}$$

Hodowany et al. have studied the energy conversion rate during SHPB test of 2024-T3 aluminum alloy with the strain rate of 3000 s^{-1}. It is found that the energy conversion rate varies with the strain, as shown in Fig. 8.

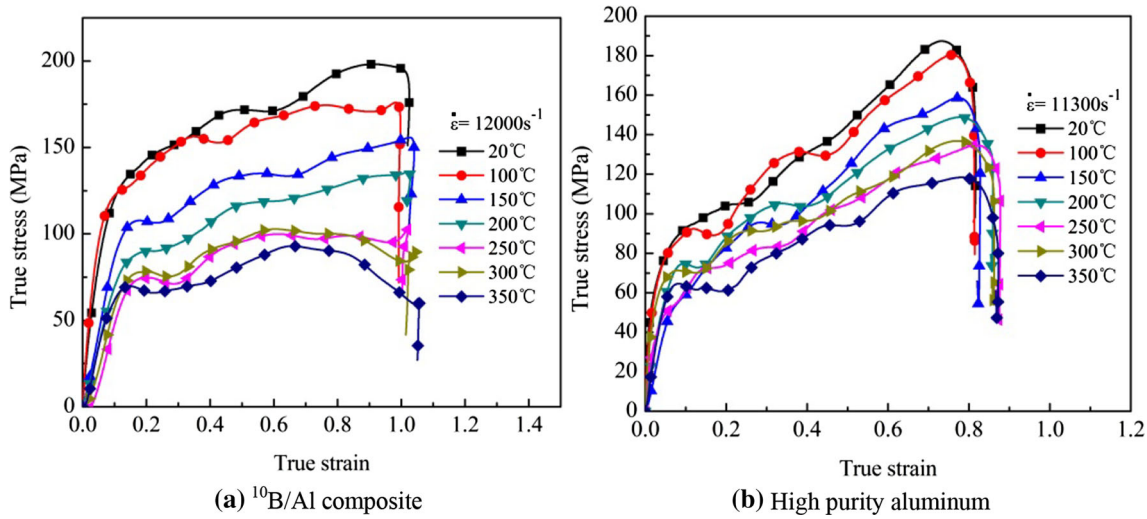

(a) ^{10}B/Al composite **(b)** High purity aluminum

Figure 6 The true strain–strain curves of different temperatures in the strain rate of 12000 s^{-1}.

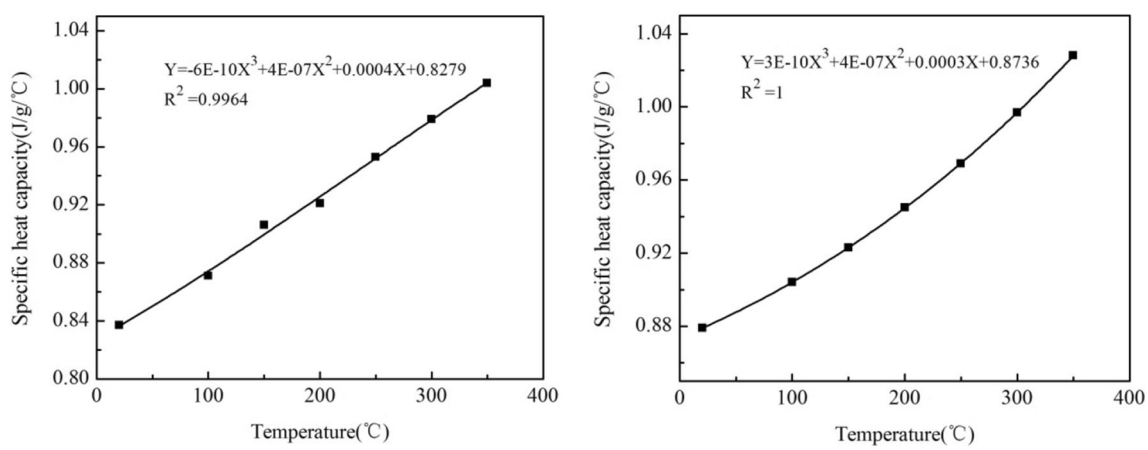

(a) ^{10}B/Al composite **(b)** High purity aluminum

Figure 7 The specific heat capacity at the different temperatures.

For the calculation of adiabatic temperature rise ΔT in this study, the curve in Fig. 8 is presented as follows:

$$\begin{aligned} &\beta = 0.30 && \varepsilon_E < 0.20 \\ &\beta = 2.75\varepsilon_T - 0.25 && 0.20 \le \varepsilon_T \le 0.44 \\ &\beta = 0.96 && \varepsilon_T > 0.44 \end{aligned} \tag{10}$$

The theoretical adiabatic temperature rise can be calculated from Eq. (7). The curve of adiabatic temperature rise with various strains could be calculated by trapezoidal integration method to consider the coupling relationship between the adiabatic temperature rise and the temperature-depended specific heat capacity. The adiabatic temperature rise of different temperatures in the strain rate around 3000 s^{-1} is shown in Fig. 8. And the adiabatic temperature rise of different temperatures in the strain rate around 12000 s^{-1} is shown in Fig. 9.

With the increase in temperature, the decrease in true stress leads to the decrease in adiabatic temperature rise. The adiabatic temperature rise has a significant impact on true stress [23, 24]. With the increase in impact pressure, the strain rate of material deformation increases, while the maximal strain increases, which leads to the obvious increase in adiabatic temperature rise. The adiabatic temperature rise of ^{10}B/Al composite is a little higher than that of high-purity aluminum at the strain rate of 3000 s^{-1}. But the adiabatic temperature rise of ^{10}B/Al composite is much higher than that of high-purity aluminum at the strain rate of 12000 s^{-1}. The adiabatic temperature rise at the strain rate of 3000 s^{-1} is lower

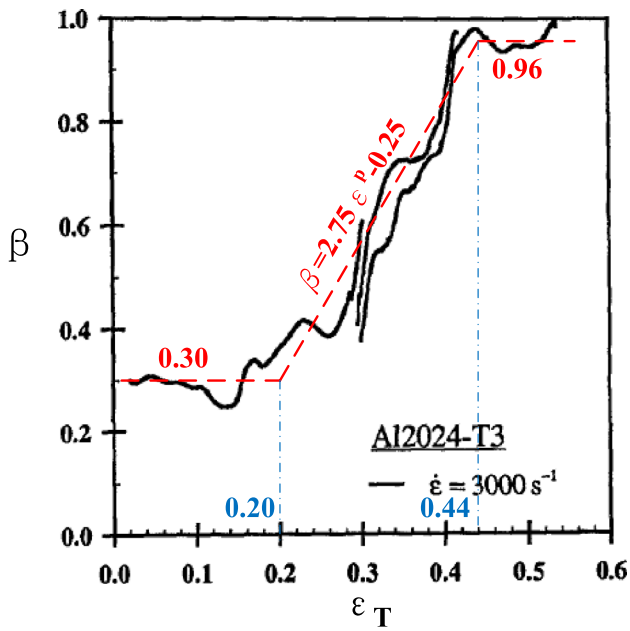

Figure 8 The energy conversion rate in the different strain [22].

than 5 °C, which is even ignored, while the maximal adiabatic temperature rise at the strain rate of 12000 s^{-1} is 64.8 °C for $^{10}B/Al$ composite and 40.1 °C for high-purity aluminum. The adiabatic temperature rise reflects the local temperature during machining processes, and the local temperature greatly influences the geometrical precision of precision machined parts. And the local temperature is difficult to be lowered by regular cooling technology [25]. So the cutting speed of machining processes should be controlled in a lower level to decrease the strain rate of workpiece material.

Isothermal stress–strain curves

As mentioned in "The adiabatic temperature rise" section, the temperature in the experimental stress–strain curves of every strain is different. So it is difficult to analyze the influence of strain rate or temperature in the same condition. The experimental stress–strain curves should be switched to the isothermal curves. The total deformation temperatures T_{def}, which are defined as the sum of room temperature T_{room} and adiabatic temperature rise ΔT, and the thermal softening coefficient should be provided for the calculation of isothermal curves. When the initial temperature is set as room temperature and the adiabatic temperature rise in the different conditions is shown in Figs. 9 and 10, the total deformation temperatures are determined. The thermal softening coefficient is determined by the stress at the different temperatures in the strain rate of 3000 s^{-1} for $^{10}B/Al$ and 3300 s^{-1} for high-purity aluminum when the adiabatic temperature rise in low strain rate (about 3000 s^{-1}) is ignored.

The true stresses in Fig. 5 are averaged in the strain scope from 0.08 to 0.12, as shown in Fig. 11.

The thermal softening coefficients are expressed by polynomial fitting, as shown in Fig. 12. The thermal softening coefficients in the room temperature are defined as 1.

The mathematical expression of the thermal softening coefficients $\Theta(T)$ for $^{10}B/Al$ composite is as follows:

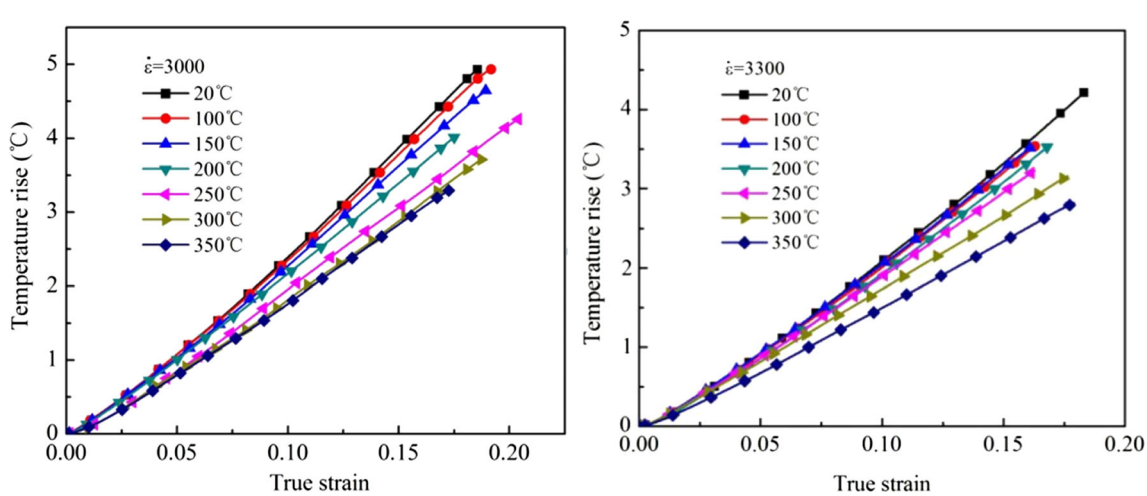

(a) $^{10}B/Al$ composite **(b)** High purity aluminum

Figure 9 The adiabatic temperature rise of different temperatures in the strain rate around 3000 s^{-1}.

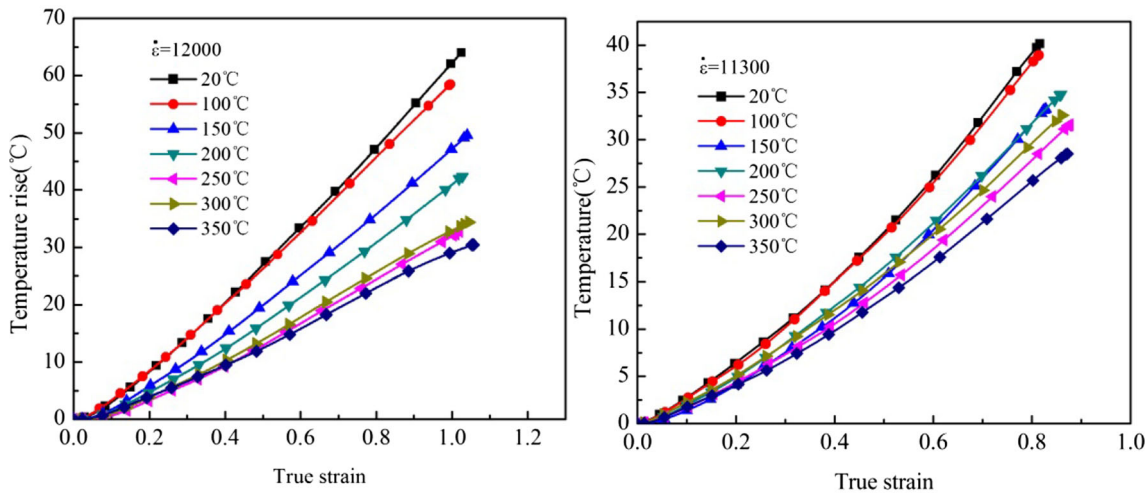

(a) ^{10}B/Al composite **(b)** High purity aluminum

Figure 10 The adiabatic temperature rise of different temperatures in the strain rate around 12000 s^{-1}.

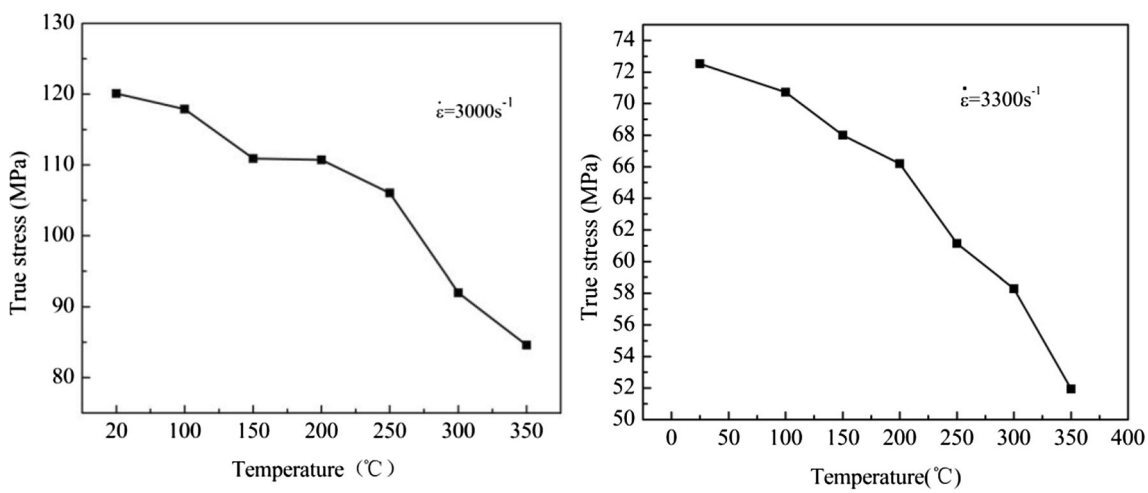

(a) ^{10}B/Al composite **(b)** High purity aluminum

Figure 11 The averaged true stress in the strain scope from 0.08 to 0.12.

$$\Theta(T) = 1.008 - 3.608\mathrm{E}^{-4}T + 6.283\mathrm{E}^{-7}T^2 - 6.105\mathrm{E}^{-9}T^3 \tag{11}$$

The mathematical expression of the thermal softening coefficients $\Theta(T)$ for high-purity aluminum is as follows:

$$\Theta(T) = 1.013 - 1.9038\mathrm{E}^{-4}T - 1.163\mathrm{E}^{-6}T^2 - 1.746\mathrm{E}^{-9}T^3 \tag{12}$$

The isothermal stress σ_i in the different strain is calculated as:

$$\sigma_\mathrm{i} = \sigma_\mathrm{T} E \Theta(T_\mathrm{def}) \tag{13}$$

The comparison of isothermal curves and original curves is shown in Fig. 13. A difference is shown that cannot be ignored, which explains the necessity for the above correction.

After switching to the isothermal curves, the sensitivity of strain rate on the true stress is analyzed more accurately. Figure 14 shows the average true stress of strain from 0.08 to 0.12 at the different strain rates. It is found that ^{10}B/Al composite and high-purity aluminum materials have strong strain rate sensitivity; namely, the true stress significantly increases with the increase in strain rate. It is presented that the main reason for this phenomenon is the dislocation sticking effect of the material during

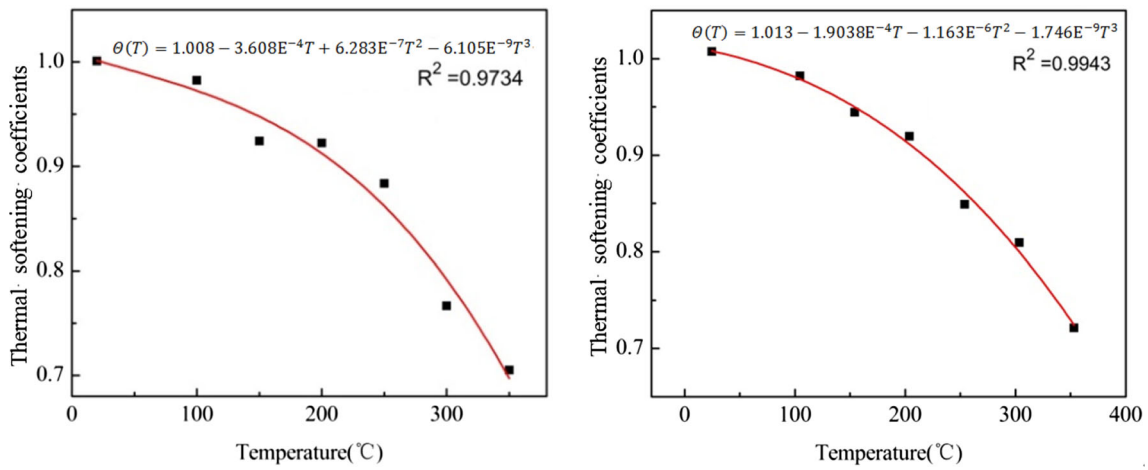

(a) ^{10}B/Al composite **(b)** High purity aluminum

Figure 12 The thermal softening coefficients (strain rate 3000 s^{-1}).

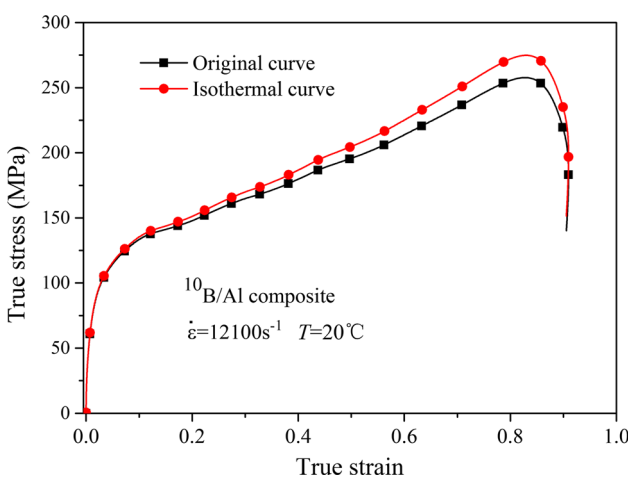

Figure 13 The comparison between before correction and after correction.

high strain rate deformation [26]. The strain rate sensitivity of high-purity aluminum is strong in the strain rate beyond 9000 s^{-1}, and the strain rate sensitivity is weakened when the strain rate is lower than 9000 s^{-1}. The reason is that the material flow is greatly limited by the dislocation sticking. However, the strain rate sensitivity of ^{10}B/Al composite is strong in the strain rate below 6000 s^{-1}, and the strain rate sensitivity is weakened when the strain rate is higher than 6000 s^{-1}.

The section of specimen after impact in the strain rate of 2800 s^{-1} and 12100 s^{-1} has been processed to investigate the material deformation condition, especially the interface between particles and matrix, as shown in Fig. 15.

It is found that the interface between particles and matrix failures in the high strain rate due to the impact effect. The impact energy could be dissipated during the crack propagation process, rather than material dislocation. So the strain rate sensitivity weakens. When the interface between particles and matrix keeps integrity, the interface strengthens the dislocation sticking, which obviously increases the strength of materials. The high strain rate, which could relate to the high cutting speed during machining processes, influences the structural integrity of ^{10}B/Al composite, which is harmful to the part life. For high-purity aluminum, the strong strain rate sensitivity leads to the increase in cutting forces and temperature in the high speed machining processes, which results in the geometrical error of machined parts.

Constitutive modeling of ^{10}B/Al composite and high-purity aluminum

Selection of constitutive models

There are many kinds of constitutive models for describing material deformation behavior [27]. Among these models, the Johnson–Cook model and the power-law model are simpler and more effective for the industrial applications, compared with other constitutive models [28].

The expression of power-law model is as follows:

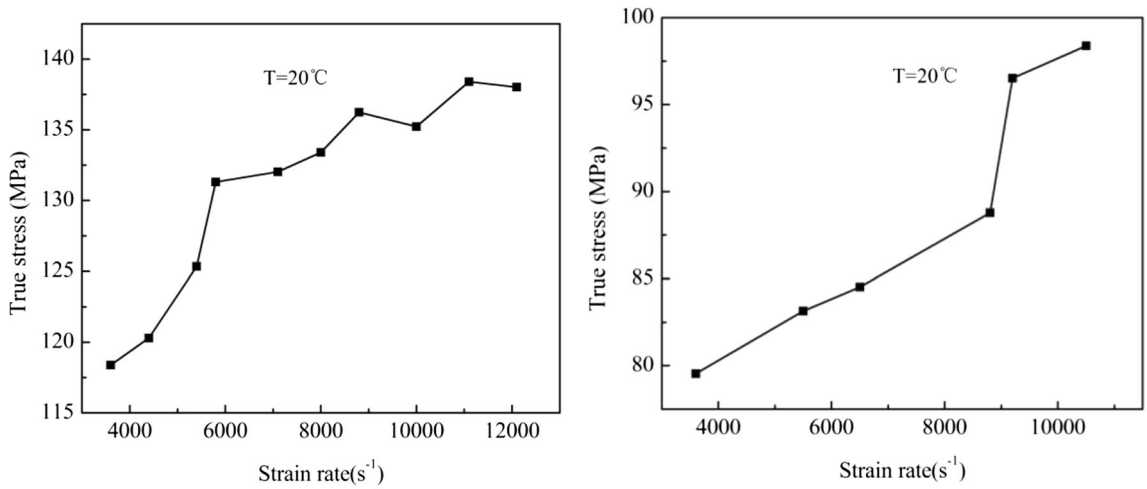

(a) ^{10}B/Al composite **(b)** High purity aluminum

Figure 14 The strain rate sensitivity in the room temperature.

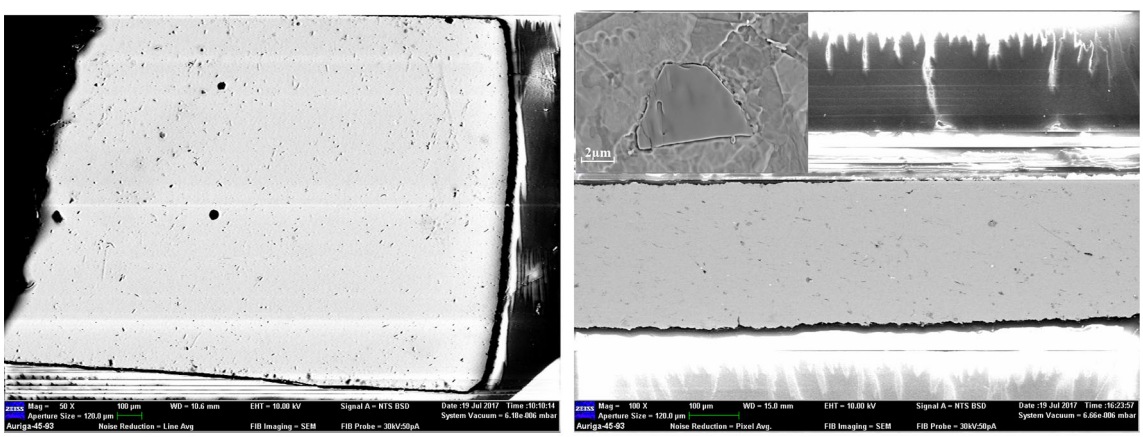

(a) strain rate of 2800 s^{-1} **(b)** strain rate of 12000 s^{-1}

Figure 15 The specimen section after impact and the interface analysis.

$$\sigma(\varepsilon_T, \dot{\varepsilon}_T, T) = \sigma_0\left(1+\frac{\varepsilon_T}{\varepsilon_{E0}}\right)^N \cdot \left(1+\frac{\dot{\varepsilon}_T}{\dot{\varepsilon}_{T0}}\right)^M \cdot \left(c_0 + c_1 T + c_2 T^2 + c_3 T^3\right) \tag{14}$$

And the expression of Johnson–Cook model is as follows:

$$\sigma(\varepsilon_T, \dot{\varepsilon}_T, T) = \left(A + B\cdot\varepsilon_T^n\right)\cdot\left(1 + C\ln\dot{\varepsilon}_T\right) \cdot \left(1 - \left(\frac{T - T_{room}}{T_{melt} - T_{room}}\right)^m\right) \tag{15}$$

where N, M and c_0–c_3 are the constants for the power-law model; A, B, C, n and m is the constants for the Johnson–Cook model ; T_{room} is the room temperature and T_{melt} is the melt point of material.

Parameters of constitutive models and their error analysis

The data of isothermal strain–stress curves are employed to fit the power-law model and Johnson–Cook model, respectively.

The constitutive models for ^{10}B/Al composite are as follows:

$$\sigma(\varepsilon_T, \dot{\varepsilon}_T, T) = 67.16\left(1+\frac{\varepsilon_T}{0.0012}\right)^{0.1334} \cdot \left(1+\frac{\dot{\varepsilon}_T}{10000}\right)^{0.2044} \cdot \times \left(1.008 - 3.608E^{-4}T + 6.283E^{-7}T^2 - 6.105E^{-9}T^3\right) \tag{16}$$

Table 2 ^{10}B/Al composite constitutive model prediction error analysis (room temperature)

Strain rate (s^{-1})	ε_t	σ_T (MPa)	PL-σ_T (MPa)	JC-σ_T (MPa)	PL-error (%)	JC-error (%)
2800	0.04	100.28	111.79	101.12	11.5	0.8
	0.08	115.02	123.16	112.45	7.1	2.2
	0.12	125.89	130.10	120.12	3.3	4.6
3600	0.05	97.31	111.96	107.79	15.1	10.8
	0.15	110.84	122.81	120.32	10.8	8.5
	0.2	124.94	129.46	128.77	3.6	3.1
4400	0.1	115.21	130.04	123.16	12.9	6.9
	0.15	125.46	137.33	131.81	9.5	5.1
	0.2	142.58	142.66	138.37	0.1	3.0
5400	0.1	124.47	131.81	126.02	5.9	1.2
	0.2	148.21	144.60	141.50	2.4	4.5
	0.3	159.37	152.41	151.11	4.4	5.2
7100	0.1	130.50	134.69	130.12	3.2	0.3
	0.2	156.63	156.38	164.70	0.2	5.2
	0.3	165.56	155.75	156.14	5.9	5.7
8000	0.2	145.72	148.94	147.98	2.2	1.6
	0.3	156.63	157.01	158.18	0.2	1.0
	0.4	174.54	162.84	165.20	6.7	5.3
9200	0.2	135.87	150.94	150.63	11.1	10.9
	0.4	167.51	165.00	168.22	1.5	0.4
	0.6	186.72	173.39	176.95	7.1	5.2
11100	0.2	150.64	153.78	153.35	2.1	1.8
	0.4	181.36	168.06	170.89	7.3	5.8
	0.6	216.36	176.54	178.84	18.4	17.3
12100	0.3	164.92	163.60	165.23	0.8	0.2
	0.5	195.89	174.37	177.36	11.0	9.5
	0.7	234.99	181.34	182.21	22.8	22.5
Averaged error					6.93	5.50

$$\sigma(\varepsilon_T, \dot{\varepsilon}_T, T) = \left(67.16 + 9.238 \cdot \varepsilon_T^{0.3938}\right) \cdot (1 + 0.1245 \ln \dot{\varepsilon}_T) \cdot \left(1 - \left(\frac{T - 20}{562}\right)^{1.7391}\right) \tag{17}$$

The constitutive models for high-purity aluminum are as follows:

$$\sigma(\varepsilon_T, \dot{\varepsilon}_T, T) = 35.11\left(1 + \frac{\varepsilon_T}{0.001}\right)^{0.1784} \cdot \left(1 + \frac{\dot{\varepsilon}_T}{10000}\right)^{0.1277} \cdot \left(1.013 - 1.9038E^{-4}T - 1.163E^{-6}T^2 - 1.746E^{-9}T^3\right) \tag{18}$$

$$\sigma(\varepsilon_T, \dot{\varepsilon}_T, T) = \left(35.11 + 6.165 \cdot \varepsilon_T^{0.4333}\right) \cdot (1 + 0.9290 \ln \dot{\varepsilon}_T) \cdot \left(1 - \left(\frac{T - 20}{663}\right)^{2.0161}\right) \tag{19}$$

The prediction error of the power-law and Johnson–Cook constitutive models of the ^{10}B/Al composite and the high-purity aluminum constitutive model is calculated by Eq. (20), and the results are listed in Tables 2 and 3.

$$\text{Error} = \frac{|\sigma_T - \sigma_p|}{\sigma_T} \cdot 100\% \tag{20}$$

where ε_t is the strain and σ_T and σ_p represent the measured and predicted true stresses, respectively.

As shown in Tables 2 and 3, the fitting precision of power-law model and Johnson–Cook model is high, with the averaged error that is lower than 8%. The fitting accuracy of the Johnson–Cook model is a little higher than that of power-law model.

Conclusions

1. The true stress of ^{10}B/Al composite is more than 50% higher than the flow stress of pure aluminum because of the grain refinement of ^{10}B/Al composite due to the additive of boron particles.

Table 3 High-purity aluminum constitutive model prediction error analysis (room temperature)

Strain rate (s^{-1})	ε_t	σ_T (MPa)	PL-σ_p (MPa)	JC-σ_p (MPa)	PL-error (%)	JC-error (%)
3000	0.04	66.29	70.43	65.63	6.2	1.0
	0.08	71.28	79.85	76.39	12.0	7.2
	0.12	85.95	85.88	84.13	0.1	2.1
5500	0.1	76.80	85.01	84.98	10.7	10.6
	0.2	99.40	96.21	100.91	3.2	1.5
	0.3	110.55	103.34	111.89	6.5	1.2
6500	0.1	85.52	85.72	86.19	0.2	0.8
	0.2	96.37	96.98	102.34	0.6	6.2
	0.3	110.97	104.18	113.49	6.1	2.3
8800	0.1	87.49	87.17	88.44	0.4	1.1
	0.3	109.10	105.94	116.50	2.9	6.8
	0.5	134.91	115.77	132.12	14.2	2.1
9200	0.1	94.47	87.37	88.67	7.5	6.1
	0.3	113.77	106.20	116.67	6.7	2.6
	0.5	141.75	116.03	132.06	18.1	6.8
10500	0.2	104.59	99.68	106.33	4.7	1.7
	0.4	129.95	112.62	126.69	13.3	2.5
	0.6	160.98	120.69	138.88	25.0	13.7
Averaged error					7.69	4.24

Moreover, the boron particles increase the difficulty of dislocation movement due to pinning and sticking effect.

2. The adiabatic temperature rise at the strain rate of 3000 s^{-1} is lower than 5 °C, which is even ignored. But the adiabatic temperature rise of $^{10}B/Al$ composite is much higher than that of high-purity aluminum at the strain rate of 12000 s^{-1}.
3. Both the $^{10}B/Al$ composite and the high-purity aluminum have strong strain rate sensitivity. The strain rate sensitivity of high-purity aluminum is strong in the strain rate beyond 9000 s^{-1}, and the strain rate sensitivity is weakened when the strain rate is lower than 9000 s^{-1}. However, the strain rate sensitivity of $^{10}B/Al$ composite is strong in the strain rate below 6000 s^{-1}, and the strain rate sensitivity is weakened when the strain rate is higher than 6000 s^{-1}.
4. The constitutive models of power-law and Johnson–cook have been used to fit the experimental results. The fitting precision of power-law model and Johnson–Cook model is high, with the averaged error that is lower than 8%. The fitting accuracy of the Johnson–Cook model is a little higher than that of power-law model.

Funding

The funding was provided by National Natural Science Foundation of China (Grand No. 51475173).

References

[1] Zhu Y, Cheng H, Wang Y, An R (2019) Effects of carbon and silicon on microstructure and mechanical properties of pressureless sintered B4C/TiB2 composites. J Alloy Compd 772:537–545

[2] Kala H, Mer KKS, Kumar S (2014) A review on mechanical and tribological behaviors of stir cast aluminum matrix composites. Procedia Maters Sci 6:1951–1960

[3] Rojas JI, Siva BV, Sahoo KL, Crespo D (2018) Viscoelastic behavior of a novel aluminum metal matrix composite and comparison with pure aluminum, aluminum alloys, and a composite made of Al–Mg–Si alloy reinforced with SiC particles. J Alloys Compd 744:445–452

[4] Wang T, Chen Z, Fu H, Xu J, Fu Y, Li T (2011) Grain refining potency of Al–B master alloy on pure aluminum. Scr Mater 64:1121–1124

[5] Wu X, Li L, He N, Zhao G, Jiang F, Shen J (2018) Study on the tool wear and its effect of PCD tool in micro milling of tungsten carbide. Int J Refract Met Hard Mater 77:61–67

[6] Lin YC, Chen XM (2011) A critical review of experimental results and constitutive descriptions for metals and alloys in hot working. Mater Des 32:1733–1759

[7] Lin YC, Li LT, Jiang YQ (2012) A phenomenological constitutive model for describing thermo-viscoplastic behavior of Al–Zn–Mg–Cu alloy under hot working condition. Exp Mech 52:993–1002

[8] Lin YC, Fu YX, Jiang YQ (2012) Hot compressive deformation behavior of 7075 Al alloy under elevated temperature. J Mater Sci 47:1306–1318. https://doi.org/10.1007/s10853-011-5904-y

[9] Hao Z, Ji F, Fan Y, Lin J, Liu X, Gao S (2017) Flow characteristics and constitutive equations of flow stress in high speed cutting alloy 718. J Alloy Compd 728:854–862

[10] Ghandehariun A, Kishawy H, Balazinski M (2016) On machining modeling of metal matrix composites: a novel comprehensive constitutive equation. Int J Mech Sci 107:235–241

[11] Wu C, Zhang J, Luo G, Shen Q, Gan Z, Liu J, Zhang L (2019) Interfacial segregation and precipitates behavior in the ultrafine grained Al-based metal matrix composites. J Alloy Compd 770:625–630

[12] Zhou L, Cui C, Zhang PF, Ma ZY (2016) Finite element and experimental analysis of machinability during machining of high-volume fraction SiCp/Al composites. Int J Adv Manuf Technol 91:1–10. https://doi.org/10.1007/s00170-016-9933-1

[13] Xu J, El Mansori M (2016) Cutting modeling of hybrid CFRP/Ti composite with induced damage analysis. Materials 9:22

[14] Taya M, Arsenault RJ (1989) Metal matrix composites: thermomechanical behavior. Elsevier Science, Burlington. https://doi.org/10.1016/0921-5093(91)90405-C

[15] Song J, Guo Q, Ouyang Q, Su Y, Zhang J, Lavernia EJ, Schoenung JM, Zhang D (2015) Influence of interfaces on the mechanical behavior of SiC particulate-reinforced Al–Zn–Mg–Cu composites. Mater Sci Eng, A 644:79–84

[16] Davies EDH, Hunter SC (1963) The dynamic compression testing of solids by the method of the split Hopkinson pressure bar. J Mech Phys Solids 11:155–179

[17] Jiang F, Luan X, Wang N, Xu X, Lu X, Wen Q (2018) Research on the dynamic mechanical properties of C-plane sapphire under impact loading. Ceram Int 44:9839–9847

[18] Pang JHL, Che FX (2006) Drop impact analysis of Sn–Ag–Cu solder joints using dynamic high-strain rate plastic strain as the impact damage driving force. Electron Compon Technol Conf. https://doi.org/10.1109/ECTC.2006.1645625

[19] Yu J, Feng J, Rong Y, Xie H, Tao S (2014) Numerical study the flow stress in the machining process. Int J Adv Manuf Tech 74:509–517

[20] Luan X, Jiang F, Wang N, Xu X, Lu X, Wen Q (2018) The mechanical response characteristics of sapphire under dynamic and quasi-static indentation loading. Ceram Int 44:15208–15218

[21] Wu ZQ, Ding H, Li HY, Huang ML, Cao FR (2013) Microstructural evolution and strain hardening behavior during plastic deformation of Fe–12Mn–8Al–0.8C steel. Mater Sci Eng A Struct Mater Prop Microstruct Process 584:150–155. https://doi.org/10.1016/j.msea.2013.07.023

[22] Hodowany J, Ravichandran G, Rosakis AJ, Rosakis P (2000) Partition of plastic work into heat and stored energy in metals. Exp Mech 40:113–123

[23] Su X, Wang G, Li J, Rong Y (2016) Dynamic mechanical response and a constitutive model of Fe-based high temperature alloy at high temperatures and strain rates. Springerplus 5:504

[24] Bo S, Chen W, Yanagita T, Frew DJ (2005) Temperature effects on dynamic compressive behavior of an epoxy syntactic foam. Compos Struct 67:289–298

[25] Liu J, Chou YK (2007) On temperatures and tool wear in machining hypereutectic Al–Si alloys with vortex-tube cooling. Int J Mach Tool Manuf 47:635–645

[26] May J, Höppel HW, Göken M (2005) Strain rate sensitivity of ultrafine-grained aluminium processed by severe plastic deformation. Scr Mater 53:189–194

[27] Liang R, Khan AS (1999) A critical review of experimental results and constitutive models for BCC and FCC metals over a wide range of strain rates and temperatures. Int J Plast 15:963–980

[28] Zhang T, Jiang F, Yan L, Xu X (2018) FEM modeling of the relationship between the high-temperature hardness and high-temperature. Quasi-Static Compress Exp Mater 11:34

Publisher's Note Springer Nature remains neutral with regard to jurisdictional claims in published maps and institutional affiliations.